




Dyadic aggregated autoregressive (DASAR) model for time-frequency representation of biomedical signals

Marco A. Pinto Orellana ^{a,*}, Habib Sherkat^a, Peyman Mirtaheri ^a, Hugo L. Hammer ^{b,c}

^a*Department of Mechanical, Electronics and Chemical Engineering. Oslo Metropolitan University.*

^b*Department of Information Technology. Oslo Metropolitan University.*

^c*Department of Holistic Systems, Simula Metropolitan Center for Digital Engineering.*

Abstract

This paper introduces a new time-frequency representation method for biomedical signals: the dyadic aggregated autoregressive (DASAR) model. Signals, such as electroencephalograms (EEGs) and functional near-infrared spectroscopy (fNIRS), exhibit physiological information through time-evolving spectrum components at specific frequency intervals: 0-50 Hz (EEG) or 0-150 mHz (fNIRS). Spectrotemporal features in signals are conventionally estimated using short-time Fourier transform (STFT) and wavelet transform (WT). However, both methods may not offer the most robust or compact representation despite their widespread use in biomedical contexts. The presented method, DASAR, improves precise frequency identification and tracking of interpretable frequency components with a parsimonious set of parameters. DASAR achieves these characteristics by assuming that the biomedical time-varying spectrum comprises several independent stochastic oscillators with (piecewise) time-varying frequencies. Local stationarity can be assumed within dyadic subdivisions of the recordings, while the stochastic oscillators can be modeled with an aggregation of second-order autoregressive models (ASAR). DASAR can provide a more accurate representation of the (highly contrasted) EEG and fNIRS frequency ranges by increasing the estimation accuracy in user-defined spectrum region of interest (SROI). A mental arithmetic experiment on a hybrid EEG-fNIRS was conducted to assess the efficiency of the method. Our proposed technique, STFT, and WT were applied on both biomedical signals to discover potential oscillators that improve the discrimination between the task condition and its baseline. The results show that DASAR provided the highest spectrum differentiation and it was the only method that could identify Mayer waves as narrow-band artifacts at 97.4-97.5 mHz.

Keywords: Time-frequency representation, Multivariate time series, Electroencephalograms, Functional near-infrared spectroscopy.

1. Introduction

The brain is a complex and strongly interconnected organ with several electrical and biochemical interactions between its cellular constituents [1–3]. These interactions involve biological structures and functionalities, including vessels, glial cells (astrocytes, oligodendrocytes, and microglial), and neurons, explained by the neurovascular coupling theory [3, 4]. As a result, these brain interactions produce biomedical signals with time- and frequency-varying

*Corresponding author

properties, which can be applied for monitoring brain's pathophysiology [5] or cognitive loading [6].

This paper, focuses on the non-invasively measured biomedical time series of hemodynamic variations and electrical potentials. In the first category, functional near-infrared spectroscopy (fNIRS) is used to estimate the concentration of oxygenated hemoglobin (HbO), and its deoxygenated state (HbR) [7]. The fNIRS imaging technique uses absorbance of near-infrared (NIR) light in the blood to estimate the hemoglobin concentration. The notable difference of HbR and HbO wavelength absorption properties in the NIR region (750-850 nm) allows us to obtain a proper concentration estimation of both chromophores based on the modified Beer-Lambert law [7–9]. Electroencephalograms (EEGs), the second modality, record the electrical potential difference at several cranial locations [10]. Positive and negative charges stem as propagation of electrical waves produced by large synchronized groups of pyramidal neurons in the brain's local cortical regions [11].

Combined hemodynamic-electrical modality enhances brain-computer interface as it reflects neuron firing activities while provide information about oxygen/energy consumption in the brain's region of interest [4]. Thus it will uncover high nonlinear relationships between recordings and stimuli [12], which may result in better understanding of the working mechanisms of the brain under some diseases [13].

In both signals, features or properties extracted from time-frequency characteristics are usually conditioned on external stimuli and are used to differentiate activities. However, the time-frequency attributes are biologically distinct for the EEG and fNIRS. As an example, a common frequency fNIRS bandwidth is normally described in the range of very low-frequency waves: 10-100 mHz [14]. A typical hemodynamic response has a frequency of approximately 45 mHz ($1/22s$) [15] or 78 mHz ($1/12.75s$) during sensorimotor activities [16, 17]. On the other hand, electroencephalogram waves have a range on a broader frequency intervals: 0-50 Hz. The EEG complete spectrum is divided into five major ranges: delta (0-4 Hz), theta (4-8 Hz), alpha (8-12 Hz), beta (12-30 Hz), and gamma rhythms (> 30 Hz) [10, 18].

Consequently, two natural frameworks that would address the extraction of time-varying spectral information of biomedical signals are the short-time Fourier transform (STFT) and wavelet transform (WT). STFT has been reported for extracting patterns to measure mental workload [19], epilepsy [20] or autism spectrum disorder [21] identification, during writing [22, 23]. While WT has been employed to obtain features for glucose measurement [24], pain assessment [25, 26], artifact correction [27–29], epilepsy classification [30], or cerebral autoregulation processes [31].

As an alternative time-frequency representation, the dyadic aggregated autoregressive (DASAR) model, a novel time-frequency approach, was initially proposed in [32] as a tool to extract evolving frequency properties from modulated signals as features for automatic classification of modulation. DASAR proposes an approximation of an evolving spectrum through dyadically splitting a signal and provides an approximation of the spectrum of each segment using an aggregated second-order autoregressive model (SAR).

This paper aims to propose the use of the DASAR model as a robust alternative for the time-spectral characterization of biological signals, with a special focus on hemodynamic (fNIRS) and electrical (EEG) signals. We also extend DASAR by defining it within a formal framework based on local stationary processes, while a frequency-selectivity feature is introduced, and accompanied by an efficient estimation algorithm. By virtue of these properties, DASAR can compress the stochastic time-frequency characteristics of a signal while retaining only the strongest and main components (oscillators). In addition, DASAR offers an accurate descrip-

tion of the time-varying response of biomedical signals compared to WT and STFT, while it is maintaining its interpretable representation due to the reduced number of model's parameters.

1.1. Time-varying spectrum

A real-valued signal $x(t)$, which origins rely on a physiological process, can be assumed to have its statistical parameters smoothly changing over time under normal conditions. Therefore, it is reasonable to assume a local stationarity property on EEG [33, pp. 50-51] and fNIRS modeling [34]. Without loss of generality, we can assume $x(t)$ (sampled in an time interval $[T_0, T_1]$) to be a realization from a zero-mean stochastic process $X(t)$ with a conjugate covariance function [35, 36]

$$R(t_1, t_2) = \mathbb{E} \left[X(t_1) \overline{X(t_2)} \right] \quad (1)$$

where $\mathbb{E}[\cdot]$ is the expectation operator and $\overline{X(\cdot)}$ is the conjugate of $X(\cdot)$.

We can reformulate $R(\cdot)$ using the time distance $\Delta t = t_2 - t_1$ and the midpoint $\tau = \frac{t_2+t_1}{2}$:

$$R(t_1, t_2) = C(\tau, \Delta t) \quad (2)$$

Note that $C(\Delta t, \tau)$ is also called as the ambiguity function.

Consequently, the process $X(t)$ is defined as a wide-sense local stationary process if the covariance function can be expressed as the product of a normalized stationary covariance function $r(\Delta t)$ and non-negative instantaneous signal power function $q(\tau)$ [37]:

$$C(\tau, \Delta t) = q(\tau) r(\Delta t) \quad (3)$$

Recall that $q(\tau) = C(\Delta t = 0, \tau) \forall \tau$ and $r(\Delta t = 0) = 1$.

Martin and Flandrin defined the time-varying spectrum as the Fourier transform of $C(\tau, \Delta t)$ with respect to $\nu = \Delta t$ [38]:

$$\begin{aligned} S(\tau, \omega) &= \mathfrak{F}_{\nu \rightarrow \omega} \{C(\tau, \nu)\}(\tau, \omega) = \int_{-\infty}^{\infty} C(\tau, \nu) e^{-j\omega\nu} d\nu \\ &= \int_{-\infty}^{\infty} \mathbb{E} \left[X\left(\tau + \frac{1}{2}\nu\right) \overline{X\left(\tau - \frac{1}{2}\nu\right)} \right] e^{-j\omega\nu} d\nu \end{aligned} \quad (4)$$

Note, that the time-varying spectrum can be rearranged as the expected of the Wigner-Ville distribution $W\{\cdot\}$ over the process $X(t)$ [38]:

$$\begin{aligned} S(\tau, \omega) &= \mathbb{E} \left[\int_{-\infty}^{\infty} X\left(\tau + \frac{1}{2}\nu\right) \overline{X\left(\tau - \frac{1}{2}\nu\right)} e^{-j\omega\nu} d\nu \right] \\ &= \mathbb{E} [W\{X(t)\}] \end{aligned} \quad (5)$$

1.2. Short-time Fourier transform spectrogram

The short-time Fourier transform (STFT) of a real-valued deterministic function $h(\cdot)$, with respect to a window function $g(\cdot)$, is defined as [39]:

$$V_g(\tau, \omega) = \int_{-\infty}^{\infty} h(t) \overline{g(t-\tau)} e^{-2j\pi t\omega} dt \quad (6)$$

and the STFT spectrogram, for deterministic signals, as the squared modulus of the STFT [39]:

$$S(\tau, \omega) \equiv |V_g(\tau, \omega)|^2 \quad (7)$$

Recall that in (stochastic) stationary signals, the spectrum is defined as the Fourier transform of the autocorrelation function. In a non-stationary setting, the STFT spectrogram can be understood as the inverse Fourier transform with respect to t_2 of the Fourier transform with respect to t_1 of the conjugate covariance function (Equation 1) with respect to t_1, t_2 :

$$S(\tau, \omega) = \mathfrak{F}_{t_2 \rightarrow \omega}^{-1} \left\{ \mathfrak{F}_{t_1 \rightarrow \omega} \left\{ R(t_1, t_2) \cdot \overline{g(t_1 - \tau)} \right\}(\tau, \omega, t_2) \cdot g(t_2 - \tau) \right\}(\tau, \omega) \quad (8)$$

We can see that this formulation implies that the spectrogram is the magnitude squared of the expected STFT spectrogram. First, remark that

$$R(t_1, t_2) = \mathbb{E} \left[X(t_1) \overline{X(t_2)} \right] = \int_C \int_C X(t_1) \overline{X(t_2)} dF_X(t_1) dF_X(t_2) \quad (9)$$

where $F_X(t)$ is the cumulative distribution of X at time t with support in C :

$$\begin{aligned} S(\tau, \omega) &= \int_{-\infty}^{\infty} \int_{-\infty}^{\infty} \left(\int_C \int_C X(t_1) \overline{X(t_2)} dF_X(t_1) dF_X(t_2) \right) \cdot \\ &\quad \cdot \overline{g(t_1 - \tau)} e^{-2j\pi t_1 \omega} dt_1 g(t_2 - \tau) e^{2j\pi t_2 \omega} dt_2 \\ &= \int_C \int_C \left[\int_{-\infty}^{\infty} X(t_1) \overline{g(t_1 - \tau)} e^{-2j\pi t_1 \omega} dt_1 \right] \cdot \\ &\quad \cdot \left[\int_{-\infty}^{\infty} \overline{X(t_2)} g(t_2 - \tau) e^{2j\pi t_2 \omega} dt_2 \right] dF_X(t_1) dF_X(t_2) \\ &= \int_C \int_C \left[\int_{-\infty}^{\infty} X(t_1) \overline{g(t_1 - \tau)} e^{-2j\pi t_1 \omega} dt_1 \right] \cdot \\ &\quad \cdot \overline{\left[\int_{-\infty}^{\infty} X(t_2) g(t_2 - \tau) e^{-2j\pi t_2 \omega} dt_2 \right]} dF_X(t_1) dF_X(t_2) \\ &= \int_C \left| \int_{-\infty}^{\infty} X(t_1) \overline{g(t_1 - \tau)} e^{-2j\pi t_1 \omega} dt_1 \right|^2 \cdot \\ &\quad \cdot dF_X(t_1) \cdot \left(\int_C dF_X(t_1) \right) \end{aligned} \quad (10)$$

By simplifying the expression, we obtain the relationship between the spectrogram and the expectation of the STFT spectrogram:

$$\begin{aligned} S(\tau, \omega) &= \int_C \left| \int_{-\infty}^{\infty} X(t) \overline{g(t - \tau)} e^{-2j\pi t \omega} dt \right|^2 dF_X(t) = \int_C |V_g(\tau, \omega)|^2 dF_X(t) \\ &= \mathbb{E} \left[|V_g(\tau, \omega)|^2 \right] \end{aligned} \quad (11)$$

1.3. Wavelet spectrum

A wavelet transform is defined as the linear transformation of a function $x(t)$ into a series of rescaled and shifted wavelet basis ψ_{lk} [40] in relation to a index l and a scale k :

$$W_X(l, k) = 2^{-l/2} \int_{-\infty}^{\infty} x(t) \psi_{lk}(2^{-l}t - k) dt \quad (12)$$

In contrast with the Fourier transform, the wavelet transform decomposes a time series $x(t)$ into a series of components in time and frequency generated by manipulation of $\psi_{jk}(\cdot)$.

Chiann et al. defined the wavelet spectrum at a time index τ and scale k , with respect to the wavelet mother ψ , as [40, 41, eq. 8]

$$\eta_{lk} = \sum_{u=-\infty}^{\infty} \gamma(\tau) \Psi_{lk}(u) \quad (13)$$

where $\Psi_{lk}(u)$ is the wavelet autocorrelation function:

$$\Psi_{lk}(u) = \sum_{t=0}^{\infty} \psi_{lk}(t) \psi_{lk}(t+|u|) \quad (14)$$

In this paper, we will focus on the Morlet, or Gabor, wavelet kernel given by

$$\psi_{lk}(t) = c_0 \pi^{-\frac{1}{4}} e^{-\frac{1}{2}t^2} (e^{l\sigma t} - e^{-\frac{1}{2}\sigma^2}) \quad (15)$$

where σ is a parameter that controls the time and frequency resolution of the transform, and the c_0 is the normalization factor

$$c_0 = \frac{1}{\sqrt{1 + e^{-\sigma^2} - 2e^{-\frac{3}{4}\sigma^2}}} \quad (16)$$

Chiann proposed an unbiased estimator for P_{lk} [41], the wavelet periodogram:

$$\hat{\eta}_{lk} = \left(\sum_{t=0}^{T-1} X_t \psi_{lk}(t) \right)^2 \quad (17)$$

This estimator is unbiased when $\sum_{t=-\infty}^{\infty} (1+|t|) \gamma(t) < \infty$ [41, Thm. 1].

2. Frequency-selective dyadic aggregated autoregressive (DASAR) model

This section is dedicated to explain further details on our proposed time-varying spectrum representation. In essence, the dyadic aggregated autoregressive (DASAR) model of a real-valued signal $x(t)$, with length T , is a time-frequency representation where its time-varying spectrum $S(t, \omega)$ (Equation 4) is approximated as the weighted sum of L levels with different discontinuous spectra:

$$S_X(t, \omega) = \sum_{i=0}^L \rho(i, \omega) S^{(i)}(t, \omega) + \nu(t, \omega) \quad (18)$$

where $\nu(t, \omega)$ is an approximation error.

At a level i , $S^{(i)}(t, \omega)$ is a piece-wise spectrum constructed using localized stationary spectra estimated over a dyadic-division of the signal in the time-domain:

$$S^{(i)}(t, \omega) = \begin{cases} S_0^{(i)}(\omega) + \varepsilon_0(\omega) & 0 \leq t < \frac{T}{2^i} \\ S_1^{(i)}(\omega) + \varepsilon_1(\omega) & \frac{T}{2^i} \leq t < 2\frac{T}{2^i} \\ \vdots & \vdots \\ S_{2^i-1}^{(i)}(\omega) + \varepsilon_{2^i-1}(\omega) & T\frac{2^i-1}{2^i} \leq t < T \end{cases} \quad (19)$$

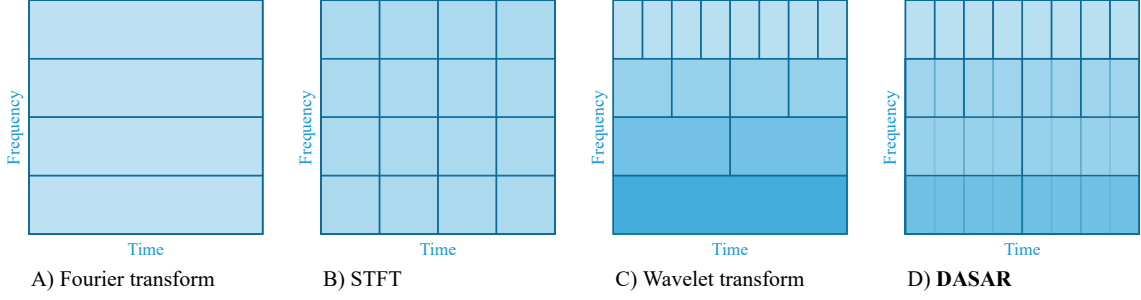


Figure 1: Time-frequency division scheme in A) Fourier transform, B) Short-time Fourier transform, C) Wavelet transform, D) Dyadic aggregated autoregressive model (DASAR)

where each piece-wise spectrum $S_j^{(i)}(\omega)$ is a aggregated second-order autoregressive model ASAR(k), i.e., the weighted sum of K stochastic oscillators described by a second-order autoregressive model SAR(ω, τ) (with a central frequency ω , a randomness τ and a *weight* $\sigma_k^{(i,j,k)}$):

$$S_j^{(i)}(t, \omega) \sim \text{ASAR}(k) = \sum_{k=1}^K \text{SAR}(\omega^{(i,j,k)}, \tau^{(i,j,k)}, \sigma_k^{(i,j,k)}) \quad (20)$$

A visual description of our time-frequency schematic division in comparison with Fourier transform, STFT or wavelet transforms is shown in Figure 1.

2.1. Local stationarity approximation

Mallat et al. defined a property for approximating local stationary processes by establishing local neighborhoods [36]. Around a point of interest t^* , let us define a neighborhood with a size $l(t^*)$, i.e. the time of analysis t is limited to the interval $t \in \mathcal{T} = [t^* - \frac{l(t^*)}{2}, t^* + \frac{l(t^*)}{2}]$. Now, calculate the decorrelation length $d(\cdot)$ in the neighborhood: the maximum distance Δt in the region \mathcal{T} with a covariance is almost close to zero. Formally, $d(t^*) = \max_{\Delta t} C(\tau, \Delta t)$, $t, t^* \in \mathcal{T}$ such that $C(\tau, \Delta t) \leq \varepsilon$ for a tolerance error ε . When the decorrelation length is upper-bounded by the neighborhood size: $d(t^*) < \frac{1}{2}l(t^*)$, we can approximate that the covariance $C(\cdot)$ by a stationary covariance $C_{t^*}(\cdot)$:

$$C(\tau, \Delta t) \approx C_{t^*}(\Delta t) \quad |\Delta t| \leq \frac{l(t^*)}{2} \quad (21)$$

Therefore, in this local region, the spectrum is defined as a function of the stationary covariance:

$$S_{t^*}(\tau) = \mathfrak{F}_{\nu \rightarrow \omega} \{C_{t^*}(\nu)\}(\omega) = \int_{-\infty}^{\infty} C_{t^*}(\nu) e^{-j\omega\nu} d\nu \quad (22)$$

Hence, we will further approximate $S_{t^*}(\tau)$ using an aggregate autoregressive model.

2.2. Autoregressive models as stochastic resonators

Stochastic oscillations in biological signals can be effectively modeled through autoregressive models [42]. Let us start modeling a single-resonator signal using an autoregressive model of second-order AR(2), or SAR. This type of autoregressive model describes a real and finite signal $x(t)$ (sampled at a fixed interval $1/f_s$) as the stochastic process generated by a linear combination of the two previous points, $x(t-1)$ and $x(t-2)$, added to an error term $\varepsilon(t)$:

$$x(t) = \phi_1 x(t-1) + \phi_2 x(t-2) + \varepsilon(t) \quad (23)$$

where ϕ_1 and ϕ_2 are known as the autoregressive coefficients. In this case, without loss of generality, we assume that $\mathbb{E}[X(t)] = 0$ with the error component modeled as a zero-mean random variable, with variance σ_ε^2 , $\varepsilon(t) \sim \mathcal{WN}(0, \sigma_\varepsilon^2)$, and serially uncorrelated $\mathbb{E}[\varepsilon(t)\varepsilon(t-u)] = 0 \forall u$.

The spectrum $S_x(\omega)$ of this stationary SAR process is characterized by:

$$S_x(\omega) = \frac{\sigma_\varepsilon^2}{|1 - \phi_1 e^{-2j\pi\omega} - \phi_2 e^{-4j\pi\omega}|^2} \quad (24)$$

where ω is the normalized frequency with respect to the sampling frequency f_s : $\omega = \frac{f}{f_s}$.

We should note that $S_x(\omega)$ has a single maximum at the dominating frequency ω^* :

$$\omega^* = \frac{1}{2\pi} \arccos\left(\frac{\phi_1(\phi_2 - 1)}{4\phi_2}\right) = \frac{1}{2\pi} \arctan\left(\frac{\phi_2}{\phi_1}\right) \quad (25)$$

when $\phi_1^2 + 4\phi_2 < 0$. Given our interest in the spectral information contained in a SAR process, we can reformulate the autoregressive coefficients based on ω^* and a parameter τ :

$$\phi_1 = \frac{2}{1 + e^{-\tau}} \cos(2\pi\omega^*) \quad (26)$$

$$\phi_2 = -\frac{1}{(1 + e^{-\tau})^2} \quad (27)$$

Therefore, SAR processes can be fully specified by the triplet $(\omega, \tau, \sigma_\varepsilon)$. In these models, τ controls the randomness of the central oscillation frequency: small values can model signals with frequency components widely spread around ω^* , and large values of τ can model signals with an clear central frequency.

Nevertheless, other autoregressive representations can have act as randomness-controlled oscillation property as well. For instance, a fourth-order autoregressive AR(4) process given by

$$x(t) = \sum_{\ell=1}^4 \phi_4 x(t-\ell) + \varepsilon(t) \quad (28)$$

have only a single resonating frequency ω^* (that is also described by Equation 25) when the autoregressive coefficients are defined as

$$\begin{pmatrix} \phi_1 \\ \phi_2 \\ \phi_3 \\ \phi_4 \end{pmatrix} = \begin{pmatrix} \frac{4}{\rho} \cos(\omega^*) \\ \frac{2}{\rho^2} (1 - 2 \cos^2(\omega^*) - 2) \\ \frac{4}{\rho^2} \cos(\omega^*) \\ -\frac{1}{\rho^4} \end{pmatrix} \quad (29)$$

where $\rho = 1 - e^{-\tau}$

AR(2), or SAR, is the lowest-order autoregressive model that can represent bandpass signals with a single maximum frequency. In order to keep an efficient parameter estimation and a compact representation, in this paper, we rely on the use of SAR models to represent stochastic oscillation behaviors.

2.3. Aggregated autoregressive model

Biomedical signals, such as EEG [10, 33, 43–46] and fNIRS [47–49] are known to have several relevant frequency components that could be associated with some physiological process. However, the above-mentioned SAR models are limited to model single-frequency systems. Nevertheless, it is possible to take advantage of the concise stochastic frequency representation offered by SAR representations and extend it towards an aggregated model, i.e., the superposition of several single-frequency stochastic models.

A general aggregated model AAR(p, K) is defined as the sum of K uncorrelated components where each one is characterized through an AR(p) process:

$$y(t) = \sum_{k=1}^K z_k(t) \quad (30)$$

where each $z_k(t)$ is a latent unobserved AR(p) time series. Some theoretical properties of these types of models were introduced by Chong et al. [50] and generalized by Dacunha-Castelle et al. for AR(p) processes [51].

We restrict to SAR models for the representation of the latent processes $z_k(t)$ in order to associate, each latent component with a central frequency ω_k^* , and a frequency randomness τ_k (Equations 26, 27, 24). In consequence, each latent process can be fully parametrized by:

$$z_k(t) = \frac{\cos(2\pi\omega_k^*)}{1 + e^{-\tau_k}} x(t) - \frac{1}{(1 + e^{-\tau_k})^2} z_k(t-1) + \varepsilon_k(t) \quad (31)$$

where ε_k is the additive white noise $\varepsilon_k \sim \mathcal{WN}(0, \sigma_{\varepsilon k}^2)$.

By definition, $z_i(t)$ and $z_j(t)$ are assumed to be uncorrelated for $i \neq j$. Therefore, the spectrum of an AAR($2, K$) process is determined by

$$S_y(\omega) = \sum_{k=1}^K \frac{\sigma_{\varepsilon k}^2}{\left| 1 - \frac{\cos(2\pi\omega_k^*)}{1+e^{-\tau_k}} e^{-2j\pi\omega} + \frac{1}{(1+e^{-\tau_k})^2} e^{-4j\pi\omega} \right|^2} \quad (32)$$

Note that for a deterministic value $\alpha \in \mathbb{R}$, scaling the latent component by $\alpha z_k(t)$ do not modify the autoregressive coefficients, but only modify the variance of $\varepsilon_k(t)$ by a factor α^2 . Therefore, to ensure identifiability, we assume that a latent component $z_k(t)$ has a unit variance, while $\sigma_{\varepsilon k}^2$ is its associated weight (Equation 20).

For brevity of notation, in the following sections, we denoted AAR($2, K$) processes as ASAR(K) models associated with a set of parameters $\{\phi_{1,1}, \phi_{2,1}, \dots, \phi_{1,K}, \phi_{2,K}, \sigma_1^2, \dots, \sigma_K^2\}$.

2.4. ASAR(K) estimation method

Estimation of the parameters in an aggregated autoregressive model is still an open problem typically addressed with Kalman filters as the main estimation algorithm. Wong et al. developed an algorithm based on expectation-maximization and Kalman filters to estimate four second-order autoregressive models (ASAR(4)) [52]. Gao et al. proposed using least-squares estimation enhanced with block resampling while relying on Kalman filtering for iterative parameter estimation for an ASAR(4) model [46]. In both cases, previous knowledge of the signal to be analyzed was required in order to define a fixed resonating frequency $\{\omega_k^*\}$. In [32], Pinto et al. introduced an iterative heuristic approach to estimate a general ASAR(K) which is only restricted by the maximum number of components or the desired approximation error.

In this paper, we introduce an improved estimation method for an ASAR (K) model that also estimates the latent components of a signal iteratively that allows to track time-varying frequency-localized changes. The following estimation algorithm relies in three main conditions:

- The signal that has a fixed, and unknown, number of main resonating frequencies with a minimum separation Δf among them, i.e, $|\omega_i - \omega_j| \leq \Delta f \ \forall i \neq j$.
- The spectrum of the signal $y(t)$ is considered appropriate with the approximation error is lower than ϵ^* .
- It is possible to explore only a particular region of the spectrum that has some biological interpretation, i.e. the spectrum region of interest (SROI) $\mathcal{W}^{(0)}$. Focalized tracking in frequency can reduce the number of iterations in the estimation algorithm while provide relevant and interpretable information. However, under lack of apriori knowledge, $\mathcal{W}^{(0)} = [0, \pi]$.

Therefore, given Δf and $\mathcal{W}^{(0)}$, we propose the following estimation algorithm composed of three stages:

1. *Estimate the spectrum using a smoothed fast Fourier transform (FFT) of $y(t)$.* The spectrum is given by $S^{(0)}(\omega) = S_X^{FFT}(\omega) = \int_{-\infty}^{\infty} \mathbb{E}[y(t)y(t-\ell)] e^{-j\pi\omega\ell} dt$ and it can be estimated using a smooth version of the FFT. We suggest the use of a median filter over the FFT of a zero-padded version of $y(t)$. Recall that zero-padding in time domain implies interpolating using a Dirichlet kernel in the frequency domain. Other smoothing filters can be used, but the obtained spectrum smoothness should not be excessive in order to avoid remove relevant frequency information.
2. *Fit an AR(2) model that describes the dominating frequency ω^* :*
 1. *Define the local neighborhood.* Let ω^* be the frequency where $S^{(k)}$ has a maximum value in the SROI $\mathcal{W}^{(k)}$:

$$\omega^* = \arg \max_{\omega \in \mathcal{W}^{(k)}} S^{(k)}(\omega), \quad \omega \in \mathcal{W}^{(k)} \quad (33)$$

Then, define a Gaussian window $B(\omega; \omega^*)$ around ω^* with a standard deviation equal to the frequency separation Δf :

$$B(\omega; \omega^*) = \kappa_B \exp\left(-\left(\frac{\omega - \omega^*}{\Delta f}\right)^2\right) \quad (34)$$

where κ_B is a normalization factor that ensures $\sum_{\omega \in W} B(\omega; \omega^*) = 1$ in the discrete set of frequencies W were estimated from the FFT algorithm. It is clear that $B(\omega; \omega^*)$ denotes the local neighborhood of the dominating frequency.

2. *Find the optimum local SAR model.* Recall that the SAR spectrum Equation 24 and $S^{(k)}$ are smooth, and therefore, with no discontinuities in their first derivative. Therefore, we can define an L_2 -distance between them in the neighborhood defined by B :

$$L(\omega^*, \tau) = \sum_{\omega} \left(S^{(k)}(\omega) B(\omega; \omega^*) - S(\omega; \omega^*, \tau) \right)^2 \quad (35)$$

The oscillation randomness $\hat{\tau}$ can be estimated by finding the minimum value of a loss function $L(\omega)$:

$$\tau^* = \arg \min_{\tau} (L(\omega^*, \tau)) \quad (36)$$

3. *Update the spectrum parameters.* The portions of spectrum that were not covered by the local SAR spectrum are updated for the following iteration:

$$S^{(k+1)}(\omega) = \left[S^{(k)}(\omega) - S(\omega; \omega^*, \tau^*) \right]^+ \quad (37)$$

and the SROI:

$$\mathcal{W}^{(k+1)} = \mathcal{W}^{(k)} \setminus \left[\omega^* - \frac{1}{2}\Delta f, \omega^* + \frac{1}{2}\Delta f \right] \quad (38)$$

4. *Repeat until convergence* when either a) the error tolerance is reached $\sum_{\omega} |S^{(k+1)}(\omega)| < \epsilon^*$; or b) all the SROI was covered, i.e., $\mathcal{W}^{(k+1)} = \emptyset$; or c) the maximum number of desired components have been estimated.

2.5. Dyadic time partition

ASAR(K) models provide a compact representation for stationary signals with a finite number of main frequencies. However, the model cannot be applied to non-stationary processes which frequency properties are changing over time. Nevertheless, we can address this issue by defining intervals where the local-stationarity property holds (Equation 4) such as we approximate the time-varying spectrum by piece-wise stationary spectra.

DASAR applies this concept by using a dyadic decomposition into levels and segments in the time-domain. A similar approach was also used in other non-stationary representations such as SLEX (smoothed localized complex exponential basis) and derived methods [53–56].

For a level i , a signal $x(t)$ with T points will be split into 2^i segments: $j = 0, 1, \dots, 2^i - 1$. Assuming local stationarity in the segment j , the spectrum can be approximated using an ASAR(K) and estimated using the algorithm of Section 2.4:

$$S_j^{(i)}(t, \omega) = \text{ASAR}(K) + \varepsilon_i(\omega) \quad (39)$$

where $\varepsilon_i(\omega)$ is a stationary zero-mean noise. Recall that this approximation is only defined on the time interval $t \in \left[k\frac{T}{2^i}, (k+1)\frac{T}{2^i} \right)$.

Note that in consequence, $S_j^{(i)}(t, \omega)$ is described by K triplets of components $\left\{ (\omega_k, \tau_k, \sigma_k^2) \right\}_{k=1}^K$ that associates a precise central frequency ω_k , its randomness τ_k and magnitude σ_k^2 of a k -th component (Section 2.3). We can improve the approximation of $S_j^{(i)}(t, \omega)$ by choosing a higher number of components K .

Thus, the spectrum (at a level i) in the interval $t \in [0, T]$ is described by the piece-wise function:

$$S^{(i)}(t, \omega) = \begin{cases} S_0^{(i)}(\omega) + \varepsilon_0(\omega) & 0 \leq t < \frac{T}{2^i} \\ S_1^{(i)}(\omega) + \varepsilon_1(\omega) & \frac{T}{2^i} \leq t < 2\frac{T}{2^i} \\ \vdots & \vdots \\ S_{2^i-1}^{(i)}(\omega) + \varepsilon_{2^i-1}(\omega) & T\frac{2^i-1}{2^i} \leq t < T \end{cases} \quad (40)$$

The accuracy of this representation will be linked to the local stationarity of the division. In wavelet transforms, the frequency bandwidth of wavelet basis assume that larger segments are more suitable to represent low-frequency spectra and shorter intervals more suitable for modeling high-frequencies [57, p. 132]. We can apply a similar principle and encode the information of each level using a non-negative weight function $\rho(i, \omega)$ that quantifies the assumed certainty of the DASAR spectrum approximation using 2^i segments at a frequency ω .

The weight function $\rho(\cdot)$ should satisfy $\sum_{i=1}^L \rho(i, \omega) = 1 \forall \omega \in \mathcal{W}^{(0)}$. Then, we can construct the full DASAR(L, K) spectrum as the sum of the piece-wise spectra $S^{(i)}(t, \omega)$ for each level i , but using the weight function $\rho(\cdot)$ for penalizing their contribution:

$$S_X(t, \omega) = \sum_{i=0}^L \rho(i, \omega) S^{(i)}(t, \omega) + \nu(t, \omega) \quad (41)$$

where $\nu(t, \omega)$ is the inherent approximation error.

3. Data validation

DASAR provides a robust framework for capturing time-varying spectral properties in a time series. In this section, we validate the model with synthetic and realistic biomedical data. We compared DASAR spectrum estimations to short-time Fourier transform (STFT) spectrograms and the wavelet transform (WT) scalograms, which served as a baseline for comparison. The synthetic data enable us to compare DASAR's ability to identify spectral changes defined *a priori*. Additionally, analysis with real biomedical signals would allow us to evaluate the method's potential to generate novel descriptive features.

3.1. Synthetic experiment with chirp signals

The first validation scenario for DASAR is a non-stationary model where the ground truth is known. For our purposes, we choose to use a chirp signal as a synthetic model in which transient patterns denote extremely non-stationary frequency modulation effects. This type of signals has been recognized as a plausible model for some physical phenomena [58, p.10-11], as well as physiological processes where it has been identified as a subject-dependent epileptic EEG biomarker [5].

In our comparison analysis, we simulate a signal consisting of a 4 Hz sinusoidal component and a sinusoidal resonator with a frequency that linearly increases from 1 Hz to 3 Hz over time:

$$y(t) = 5 \sin(8\pi t) + 5 \sin(8\pi t(1 + 0.01t)) + \frac{1}{2} \varepsilon(t) \quad (42)$$

where $\varepsilon(t)$ is a zero-mean white noise with a unit-variance.

3.2. Real experiment: concurrent EEG-fNIRS signals

The second validation phase involves evaluating DASAR's performance on real biomedical signals. In order to accomplish this, we gathered signals using a custom-built instrument capable of recording high-quality concurrent EEG-fNIRS.

The custom-built device consists of three modules: hemodynamic, biopotential, and control that capture and preprocess signals. The biopotential module's reliance on the TI-ADS1299 integrated circuit [59, 60] ensured EEG signal quality and reliability. Rashid et al. stated that, when combined with supplementary circuitry, this component may provide signal quality comparable to clinical-level EEG systems such as NuAmps (Compumedics Neuroscan copyright, Dresden, Germany) [61]. Furthermore, the hemodynamic module produces fNIRS signals, with a high signal-to-noise ratio, at three different wavelengths: 735nm, 805nm, and 850nm. The control module implemented in an integrated digital signal processing board (DSP) performs the complementary functions that interconnect and manage both modules. We refer to [62] for further details relating to the instrumentation.

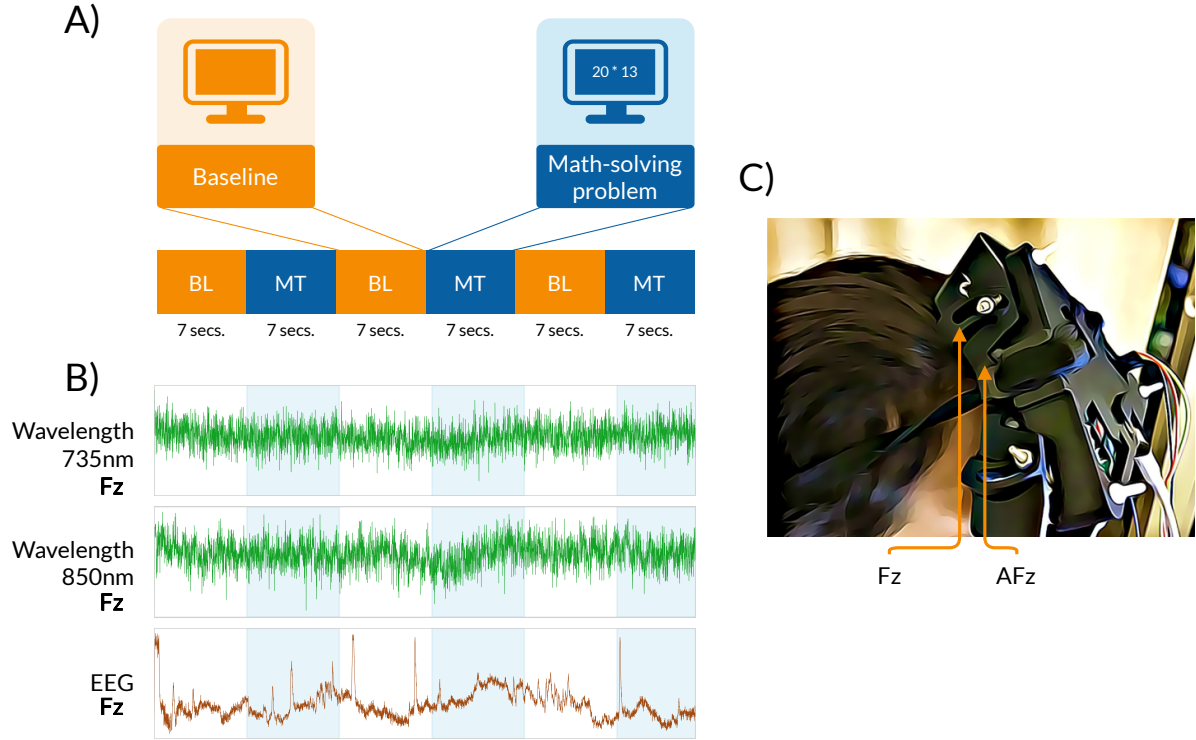


Figure 2: Experiment setup for real signal acquisition: A) experiment protocol; B) recorded biomedical signals (in normalized units); C) hybrid EEG-fNIRS montage layout.

This device was mounted, ensuring that the light source is located on the channel AFz, according to the extended 10-20 positioning system, while three photodiodes positioned at FP1, FP2, and Fz (Figure 2.C). This arrangement of light sources and detectors provides nine fNIRS channels that map the hemodynamic response on the frontal and prefrontal lobe.

EEG-fNIRS signals were collected from a single subject in the prefrontal cortex during a mental arithmetic task experiment. This family of neuropsychological activities has been extensively studied employing EEG and fNIRS [63–66]. The experiment used in this paper includes six sections alternating between arithmetic tasks and baseline intervals, where each section had an identical span of seven seconds (Figure 2). During the task period, the subject was asked to perform a two-digit subtraction, while during the baseline interval, only a cross sign was shown on the screen to keep the subject’s attention. Concentration changes in HbO and HbR were estimated from the measured light intensity of the three wavelengths using the modified Beer-Lambert law (MBBL). Two parameters of the MBBL: differential path length and extinction coefficients, were estimated using the Scholkmann model [67], and the Gratzer-Kollias model [68], respectively. Note that all the signals were recorded at a 100 Hz sampling rate.

4. Results and discussion

4.1. Synthetic chirp signal

A comparison between the estimates of the Wavelet scalogram, the STFT spectrogram, and the DASAR spectrogram applied on the synthetic data is shown in Figure 3. The three methods, as it can be observed, capture the time-varying frequency features of the chirp signal properly

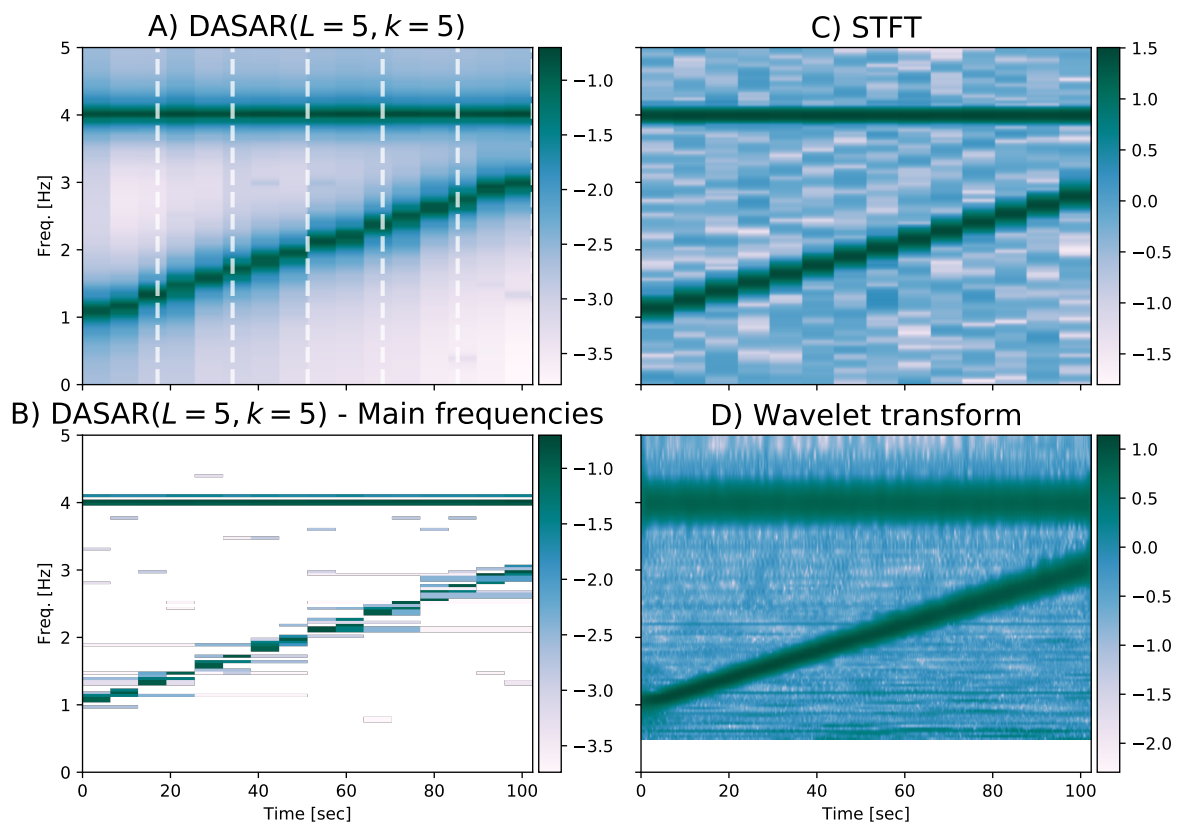


Figure 3: Comparison among time-frequency representations of a nonstationary signal: A) DASAR($L = 5, K = 5$) spectrum, B) Central frequency distribution of the DASAR($L = 5, K = 5$) model, C) Short-time Fourier transform (STFT), D) Wavelet transform. Note that magnitudes are expressed in decibels.

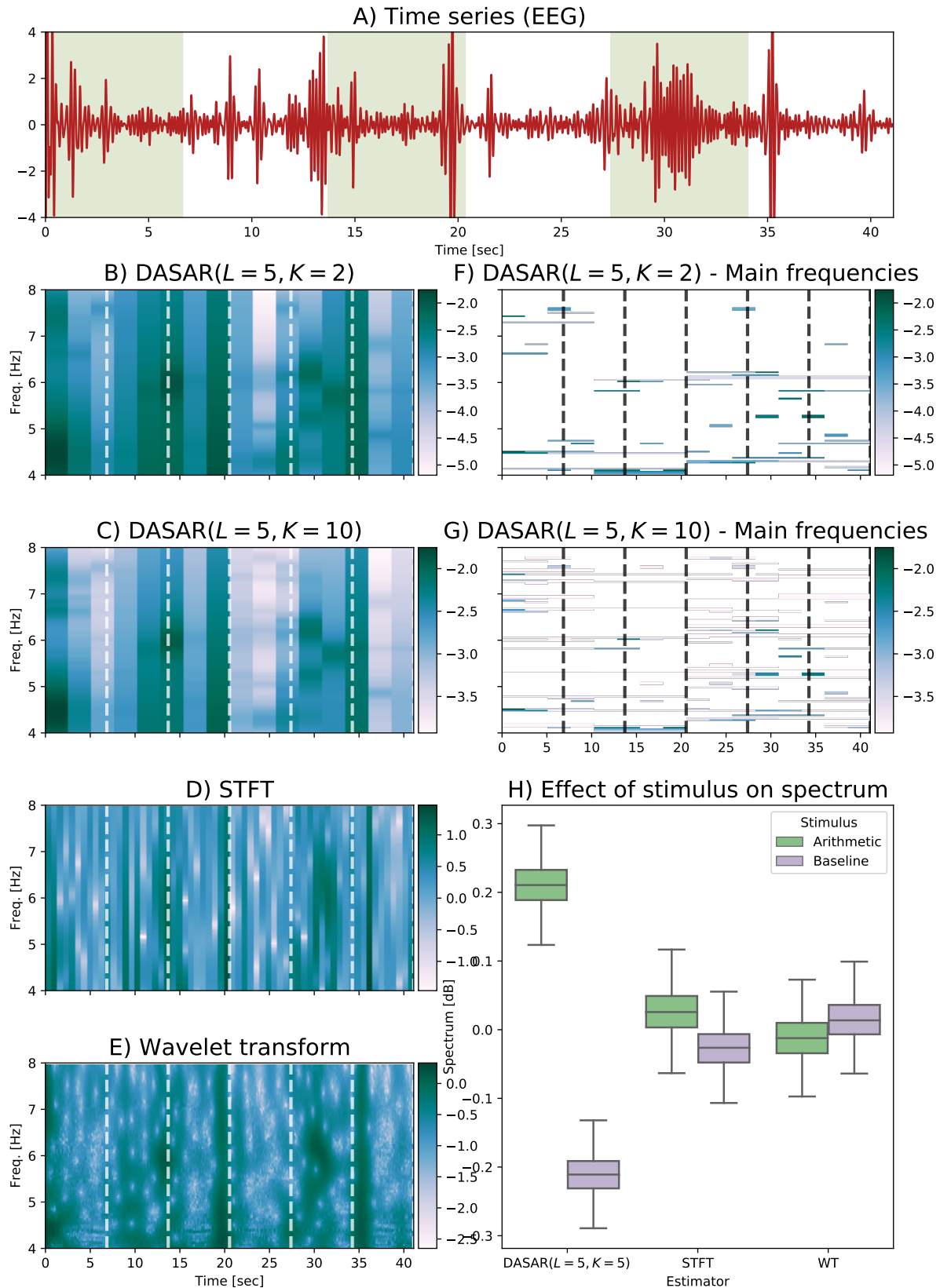


Figure 4: EEG time-frequency representations in the theta band: A) DASAR($L = 5, K = 2$) and B) DASAR($L = 5, K = 10$), C) STFT, D) WT, E) main frequencies in DASAR($L = 5, K = 2$), and F) DASAR($L = 5, K = 10$), and G) comparison of the bootstrap spectrum means between DASAR($L = 5, K = 5$), STFT and WT.

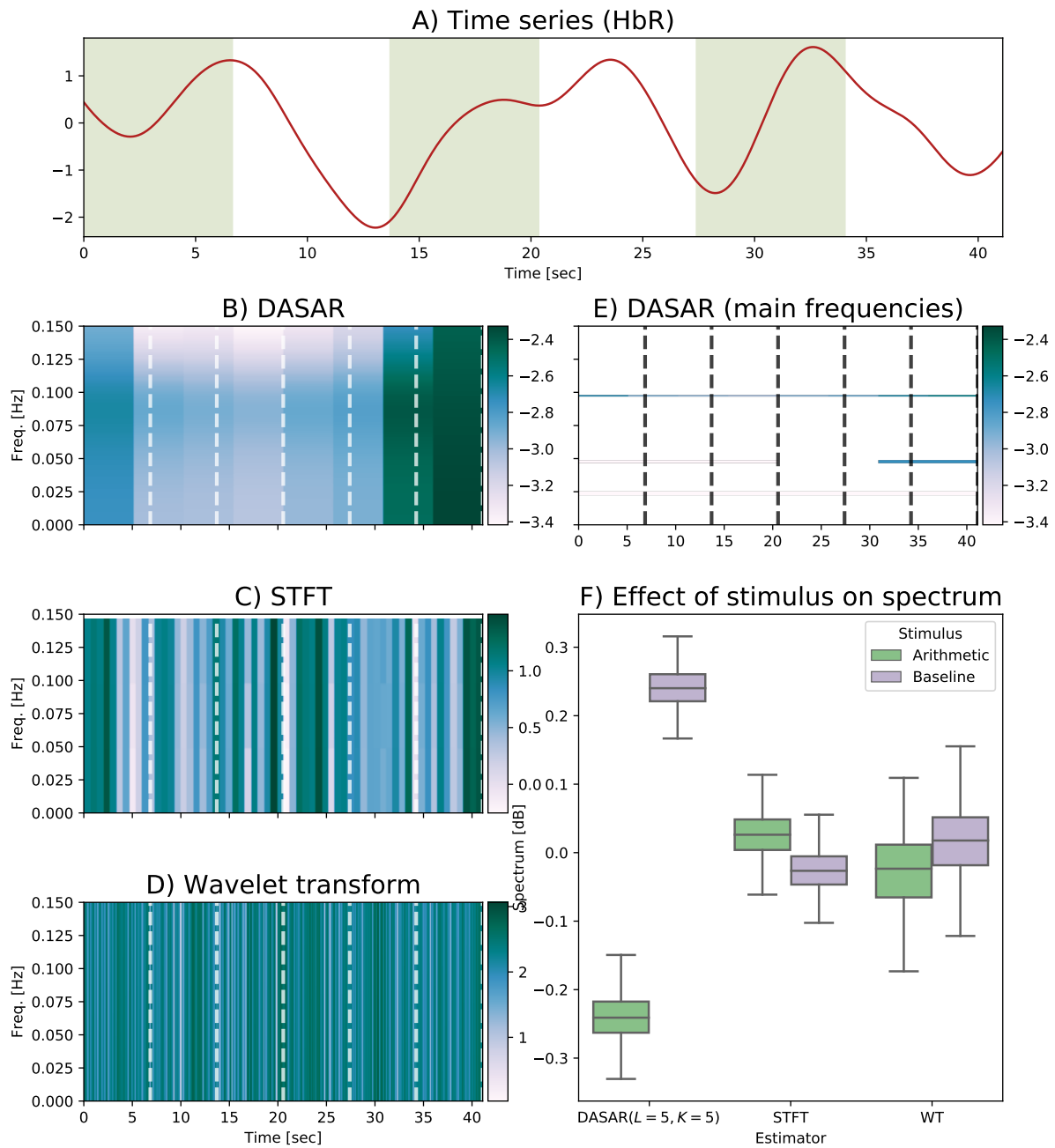


Figure 5: fNIRS-HbR time-frequency representations in the interval 0-100 mHz: A) DASAR($L = 5, K = 5$), B) STFT, C) WT, D) main frequencies in DASAR($L = 5, K = 5$), and F) their comparison of the bootstrap spectrum means.

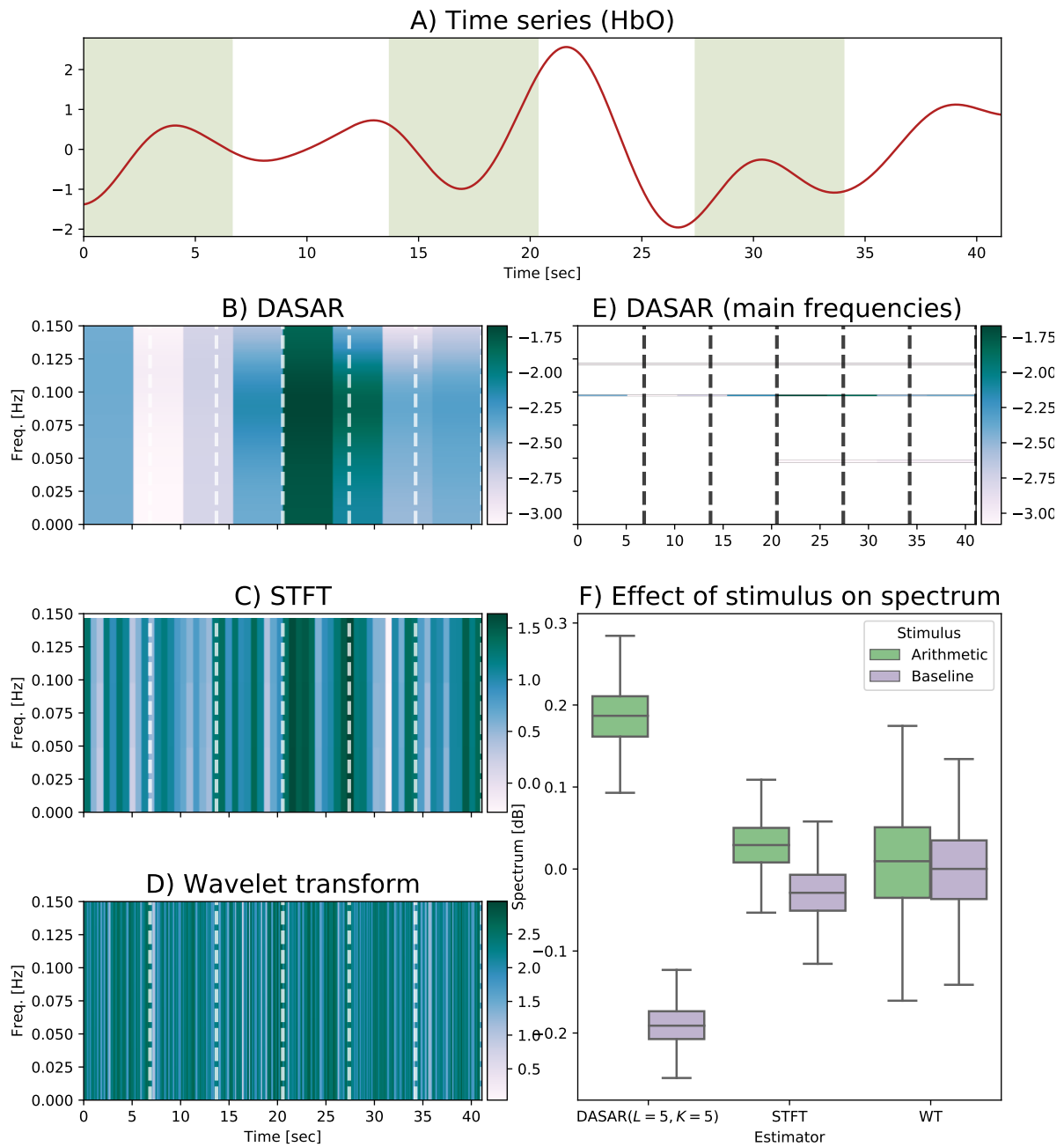


Figure 6: fNIRS-HbO time-frequency representations in the interval 0-100 mHz: A) DASAR($L = 5, K = 5$), B) STFT, C) WT, D) main frequencies in DASAR($L = 5, K = 5$), and F) their comparison of the bootstrap spectrum means.

(Figure 3.A-C). As expected, the level of precision of that identification varies according to the applied method. In comparison with STFT, DASAR spectrogram performs automatic filtering of the spurious components with a similar level achieved by the Wavelet scalogram.

A relevant feature that was outlined in this experiment is the intrinsic ability of DASAR to identify and track frequency-changing oscillators. Recall that in the DASAR interpretation of the time-varying spectrum, the spectrum at a time t is the consequence of a finite sum of oscillating components (that could suffer some randomness in their frequency). Therefore, it is possible to visualize only those critical components to evaluate their spectrum evolution in the signal (Figure 3.D). In contrast with STFT and Wavelet, DASAR allows us to identify those main components and track them without further processing: DASAR(5, 5) was able to detect the oscillator properly with a fixed frequency of 4 Hz and the component with varying frequency from 1-3 Hz (Figure 3.B). The only required assumption, in this example, was a maximum of five components per level, i.e., a combination of 25 possible frequencies per dyadic interval.

4.2. DASAR-EEG spectrogram

In the analysis of electroencephalographic signals, we focus on the EEG theta band, i.e., the 4-8 Hz frequency range. This brainwave subset seems to be correlated with cognitive arithmetic-related tasks as it was found in problem-solving activities [69], Sternberg memory scanning [70], two-digit addition [71], and two-digit multiplication problems [72]. The comparison result with STFT, wavelet, and DASAR is summarized in Figure 4.

We must recall that the DASAR model provides time-frequency representations with different accuracy levels determined by its parameters (number of levels L and oscillatory components per segment K). In this dataset, two possible time-frequency representations were used: DASAR($L = 5, K = 2$) (Figure 4.B,F) and DASAR($L = 5, K = 10$) (Figure 4.H,G). DASAR($L = 5, K = 2$) denoted only the two most relevant components capable of modeling each of the $2^L = 32$ segments in which the time series is split.

Note that DASAR models were able to analyze the spectrum dynamics that emerged exclusively within the spectrum region of interest SROI $\mathcal{W}^{(0)}$. While similar constraints can be introduced to wavelet transforms using an appropriate set of wavelet scales, this mechanism is not straightforward. In the current experiment, both DASAR models were constrained to $\mathcal{W}^{(0)} = [4, 8]$ Hz.

DASAR($L = 5, K = 2$) revealed a different estimate of the time-varying EEG spectrum (opposed to STFT and WT) with no exact main component but a high-density region in the lower theta-band: 4-6 Hz. In addition, the DASAR($L = 5, K = 10$) model (with an increased number of maximum components) was used to assist in identifying the most dominant oscillation. It showed that a faint oscillator at ~ 4.102 Hz was present during the whole session. No similar information could be drawn from the alternative time-frequency models.

Finally, we evaluated the consistency of the conclusions inferred from the three time-frequency models (DASAR, STFT, and WT) with the findings reported in the biomedical literature. For instance, Sammer et al. and Grabner et al. described an increase of the theta-band power spectrum during arithmetic tasks [71, 72]. To provide a similar metric, we standardized the magnitudes of each spectrogram (or scalogram) during the whole session, and we compared the mean spectrum for each period (arithmetic and baseline) using the bootstrap method (Figure 4.H). All time-frequency methods demonstrated an increment in the average power spectrum when the participant performed an arithmetic task. However, DASAR($L = 5, K = 5$) has exhibited the most prominent spectrum difference between both conditions.

4.3. DASAR-fNIRS spectrogram

In this paper, fNIRS data analysis was restricted to those frequency components within the range 0-150 mHz [9, 73]. This region contains biomarkers associated with autoregulatory functions and, therefore, has a biological interpretation [73]. Similar to the previous analysis, we contrasted DASAR, STFT, and WT, and the results are compiled in Figure 6 (HbO) and Figure 5 (HbR).

Frequency variations on very-low-frequency intervals are very challenging to be detected using STFT or wavelet scalograms (Figure 5.C-D and Figure 6.C-D). However, some patterns were discerned using a DASAR($L = 5, K = 5$) model: two principal components have been identified throughout most of the experiment. The strongest widespread oscillator had a central frequency in the range ~97.4-97.5 mHz, and the second oscillator was located at ~48.7 mHz. Note that in the latter, the HbR spectrogram power is higher than in HbO. On the other hand, the first oscillator is strongly correlated to Mayer waves, i.e., spontaneous biological artifacts with a similar frequency originated due to arterial blood pressure [74]. The remarkable aspect of recognizing the exact subject-dependent oscillatory frequency of the Mayer waves is the possibility of removing its effect in the signal without disrupting other physiological components at close frequencies using an anti-notch filter.

Furthermore, DASAR can provide a time-frequency representation with a small set of parameters similar to wavelet packets. In our fNIRS analysis, it is noteworthy that the time-varying parameters of two key stochastic oscillators (at the frequencies mentioned above) may be enough to explain the main information denoted in the spectrum.

Despite this information compactness, DASAR cannot ensure smooth spectral transitions across time. However, once the model is fitted, a continuous smooth spectral representation $\hat{S}_X(t, \omega)$ (Equation 18) for any normalized frequency $\omega \in [0, 1/2]$ is defined at any time point. As a consequence, DASAR does not need any additional interpolation technique as would be required in other methods that used an FFT-based estimation method, such as SLEX [54] or STFT.

5. Conclusion

We introduced the dyadic aggregated autoregressive (DASAR) model as a robust time-frequency analysis technique. This method captures the time-fluctuating spectrum characteristics of a signal by independently modeling the spectrum of signal segments with an aggregated autoregressive model. Each autoregressive component in those aggregated segment-level models can model a single stochastic oscillator, i.e., signal sources whose frequency is assumed to be unstable but located around a finite mean value. As it was shown, the lowest-degree autoregressive model that satisfies this single-oscillator property is the second-order that DASAR uses by design (it should be noted that the proposed model is not restricted to this model order). Additionally to this structure, we have introduced a spectrum region of interest (SROI) where the time-varying spectrum estimation process will be focused. As a result, SROI can provide accurate estimates in the frequency intervals where biomedical signals are recognized to have a particular interpretation.

DASAR was applied to two types of biomedical signals: electroencephalogram (EEG) and functional near-infrared spectroscopy (fNIRS) time series during a two-digit multiplication task. Both types of signals were analyzed in a separate spectral domain: the EEG processing was focused on the theta-band: 4-8 Hz, while the fNIRS analysis was concentrated in a very-low-frequency range (10-100 mHz). In both types of signals, it was observed that DASAR

increased the contrast of the mean time-varying spectrum, between both stimuli, in comparison with the short-time Fourier transform (STFT) and complex Morlet wavelet (WT). DASAR also was able to detect subtle time-varying characteristics, such as the Mayer waves that were often neglected by the alternative methods due to its frequency scale.

From the observed results, we can emphasize three main unique characteristics of DASAR in relation to STFT and WT. First, while DASAR can estimate a similar time-frequency response as the above-mentioned methods, the spectrum mean values in the fitted $ASAR(K)$ models can be used to precisely identify and track the main oscillating components. Second, DASAR allows interpretable frequency-focused tracking in the spectrum region of interest. Finally, DASAR provides coverage of the entire time-varying spectrum representation with a reduced number of parameters. Based on this characteristics on the simulated data and the realistic biomedical signals, we can suggest DASAR as an alternative time-frequency method to analyze hemodynamic and electrical time series.

References

- [1] A. Schüz, G. Palm, Density of neurons and synapses in the cerebral cortex of the mouse, *The Journal of Comparative Neurology* 286 (4) (1989) 442–455. doi:10.1002/cne.902860404.
- [2] F. Reina-De La Torre, A. Rodriguez-Baeza, J. Sahuquillo-Barris, Morphological characteristics and distribution pattern of the arterial vessels in human cerebral cortex: A scanning electron microscope study, *The Anatomical Record* 251 (1) (1998) 87–96. doi:10.1002/(SICI)1097-0185(199805)251:1<87::AID-AR14>3.0.CO;2-7.
- [3] L. Kaplan, B. W. Chow, C. Gu, Neuronal regulation of the blood-brain barrier and neurovascular coupling, *Nature Reviews. Neuroscience* 21 (8) (2020) 416–432. doi:10.1038/s41583-020-0322-2.
- [4] K. Gramann, T.-P. Jung, D. P. Ferris, C.-T. Lin, S. Makeig, Toward a new cognitive neuroscience: Modeling natural brain dynamics, *Frontiers in Human Neuroscience* 8 (2014) 444. doi:10.3389/fnhum.2014.00444.
- [5] S. J. Schiff, D. Colella, G. M. Jacyna, E. Hughes, J. W. Creekmore, A. Marshall, M. Bozek-Kuzmicki, G. Benke, W. D. Gaillard, J. Conry, S. R. Weinstein, Brain chirps: Spectrographic signatures of epileptic seizures, *Clinical Neurophysiology* 111 (6) (2000) 953–958. doi:10.1016/S1388-2457(00)00259-5.
- [6] G. G. Yener, E. Başar, Brain oscillations as biomarkers in neuropsychiatric disorders, in: *Supplements to Clinical Neurophysiology*, Vol. 62, Elsevier, 2013, pp. 343–363. doi:10.1016/B978-0-7020-5307-8.00016-8.
- [7] A. Villringer, Non-invasive optical spectroscopy and imaging of human brain function, *Trends in Neurosciences* 20 (10) (1997) 435–442. doi:10.1016/s0166-2236(97)01132-6.
- [8] D. A. Burns, E. W. Ciruczak, *Handbook of Near-Infrared Analysis*, CRC Press. Taylor & Francis Group, Boca Raton, Florida, 2008.
- [9] F. Jobsis, Noninvasive, infrared monitoring of cerebral and myocardial oxygen sufficiency and circulatory parameters, *Science* 198 (4323) (1977) 1264–1267. doi:10.1126/science.929199.
- [10] J. Stern, *Atlas of EEG Patterns*, Wolters Kluwer/Lippincott Williams & Wilkins Health, Philadelphia, 2013.
- [11] B. Khalil, *Atlas of EEG and Seizure Semiology*, Butterworth-Heinemann/Elsevier, Philadelphia, 2006.
- [12] K.-S. Hong, M. J. Khan, Hybrid Brain-Computer Interface Techniques for Improved Classification Accuracy and Increased Number of Commands: A Review, *Frontiers in Neurorobotics* 11 (2017) 35. doi:10.3389/fnbot.2017.00035.
- [13] A. Machado, J. Lina, J. Tremblay, M. Lassonde, D. Nguyen, F. Lesage, C. Grova, Detection of hemodynamic responses to epileptic activity using simultaneous Electro-EncephaloGraphy (EEG)/Near Infra Red Spectroscopy (NIRS) acquisitions, *NeuroImage* 56 (1) (2011) 114–125. doi:10.1016/j.neuroimage.2010.12.026.
- [14] P. Pinti, F. Scholkmann, A. Hamilton, P. Burgess, I. Tachtsidis, Current Status and Issues Regarding Pre-processing of fNIRS Neuroimaging Data: An Investigation of Diverse Signal Filtering Methods Within a General Linear Model Framework, *Frontiers in Human Neuroscience* 12 (Jan. 2019). doi:10.3389/fnhum.2018.00505.
- [15] W. Penny, K. Friston, J. Ashburner, S. Kiebel, T. Nichols, *Statistical Parametric Mapping: The Anal-*

- ysis of Functional Brain Images, Elsevier Science, 2011, https://books.google.no/books?id=G_qdEsDlkp0C.
- [16] G. H. Glover, Deconvolution of Impulse Response in Event-Related BOLD fMRI, *NeuroImage* 9 (4) (1999) 416–429. [doi:10.1006/nimg.1998.0419](https://doi.org/10.1006/nimg.1998.0419).
 - [17] W. Yan, D. Rangaprakash, G. Deshpande, Aberrant hemodynamic responses in autism: Implications for resting state fMRI functional connectivity studies, *NeuroImage: Clinical* 19 (2018) 320–330. [doi:10.1016/j.nicl.2018.04.013](https://doi.org/10.1016/j.nicl.2018.04.013).
 - [18] P. L. Nunez, R. Srinivasan, *Electric Fields of the Brain: The Neurophysics of EEG*, 2nd Edition, Oxford University Press, Oxford ; New York, 2006.
 - [19] H. Aghajani, M. Garbey, A. Omurtag, Measuring Mental Workload with EEG+fNIRS, *Frontiers in Human Neuroscience* 11 (Jul. 2017). [doi:10.3389/fnhum.2017.00359](https://doi.org/10.3389/fnhum.2017.00359).
 - [20] K. Samiee, P. Kovacs, M. Gabbouj, Epileptic Seizure Classification of EEG Time-Series Using Rational Discrete Short-Time Fourier Transform, *IEEE Transactions on Biomedical Engineering* 62 (2) (2015) 541–552. [doi:10.1109/tbme.2014.2360101](https://doi.org/10.1109/tbme.2014.2360101).
 - [21] H. Behnam, A. Sheikhan, M. R. Mohammadi, M. Noroozian, P. Golabi, Analyses of EEG background activity in Autism disorders with fast Fourier transform and short time Fourier measure, in: 2007 International Conference on Intelligent and Advanced Systems, IEEE, 2007. [doi:10.1109/icias.2007.4658582](https://doi.org/10.1109/icias.2007.4658582).
 - [22] A. Zabidi, W. Mansor, Y. K. Lee, C. W. N. F. C. W. Fadzal, Short-time Fourier Transform analysis of EEG signal generated during imagined writing, in: 2012 International Conference on System Engineering and Technology (ICSET), IEEE, 2012. [doi:10.1109/icsengt.2012.6339284](https://doi.org/10.1109/icsengt.2012.6339284).
 - [23] C. W. N. F. C. W. Fadzal, W. Mansor, L. Y. Khuan, A. Zabidi, Short-time Fourier Transform analysis of EEG signal from writing, in: 2012 IEEE 8th International Colloquium on Signal Processing and Its Applications, IEEE, 2012. [doi:10.1109/cspa.2012.6194785](https://doi.org/10.1109/cspa.2012.6194785).
 - [24] X. Li, C. Li, Study on the Application of Wavelet Transform to Non-invasive Glucose Concentration Measurement by NIRS, in: 2015 Fifth International Conference on Instrumentation and Measurement, Computer, Communication and Control (IMCCC), IEEE, 2015. [doi:10.1109/imccc.2015.278](https://doi.org/10.1109/imccc.2015.278).
 - [25] D. Lopez-Martinez, K. Peng, A. Lee, D. Borsook, R. Picard, Pain Detection with fNIRS-Measured Brain Signals: A Personalized Machine Learning Approach Using the Wavelet Transform and Bayesian Hierarchical Modeling with Dirichlet Process Priors, in: 2019 8th International Conference on Affective Computing and Intelligent Interaction Workshops and Demos (ACIIW), IEEE, 2019. [doi:10.1109/aciiw.2019.8925076](https://doi.org/10.1109/aciiw.2019.8925076).
 - [26] R. F. Rojas, M. Liao, J. Romero, X. Huang, K.-L. Ou, Cortical Network Response to Acupuncture and the Effect of the Hegu Point: An fNIRS Study, *Sensors* 19 (2) (2019) 394. [doi:10.3390/s19020394](https://doi.org/10.3390/s19020394).
 - [27] A. M. Chiarelli, E. L. Maclin, M. Fabiani, G. Gratton, A kurtosis-based wavelet algorithm for motion artifact correction of fNIRS data, *NeuroImage* 112 (2015) 128–137. [doi:10.1016/j.neuroimage.2015.02.057](https://doi.org/10.1016/j.neuroimage.2015.02.057).
 - [28] C. A. Joyce, I. F. Gorodnitsky, M. Kutas, Automatic removal of eye movement and blink artifacts from EEG data using blind component separation, *Psychophysiology* 41 (2) (2004) 313–325. [doi:10.1111/j.1469-8986.2003.00141.x](https://doi.org/10.1111/j.1469-8986.2003.00141.x).
 - [29] J. L. Kenemans, P. C. M. Molenaar, M. N. Verbaten, J. L. Slangen, Removal of the Ocular Artifact from the EEG: A Comparison of Time and Frequency Domain Methods with Simulated and Real Data, *Psychophysiology* 28 (1) (1991) 114–121. [doi:10.1111/j.1469-8986.1991.tb03397.x](https://doi.org/10.1111/j.1469-8986.1991.tb03397.x).
 - [30] H. Adeli, Z. Zhou, N. Dadmehr, Analysis of EEG records in an epileptic patient using wavelet transform, *Journal of Neuroscience Methods* 123 (1) (2003) 69–87. [doi:10.1016/s0165-0270\(02\)00340-0](https://doi.org/10.1016/s0165-0270(02)00340-0).
 - [31] P. S. Addison, A Review of Wavelet Transform Time–Frequency Methods for NIRS-Based Analysis of Cerebral Autoregulation, *IEEE Reviews in Biomedical Engineering* 8 (2015) 78–85. [doi:10.1109/rbme.2015.2436978](https://doi.org/10.1109/rbme.2015.2436978).
 - [32] M. A. Pinto-Orellana, H. L. Hammer, Dyadic Aggregated Autoregressive Model (DASAR) for Automatic Modulation Classification, *IEEE Access* 8 (2020) 156096–156103. [doi:10.1109/access.2020.3019243](https://doi.org/10.1109/access.2020.3019243).
 - [33] S. Sanei, J. Chambers, *EEG Signal Processing*, John Wiley & Sons, Chichester, England ; Hoboken, NJ, 2007.
 - [34] T. Fekete, D. Rubin, J. M. Carlson, L. R. Mujica-Parodi, The NIRS Analysis Package: Noise Reduction and Statistical Inference, *PLoS ONE* 6 (9) (2011) e24322. [doi:10.1371/journal.pone.0024322](https://doi.org/10.1371/journal.pone.0024322).
 - [35] A. Napolitano, *Generalizations of Cyclostationary Signal Processing: Spectral Analysis and Applications*, John Wiley & Sons, Ltd, Chichester, UK, 2012. [doi:10.1002/9781118437926](https://doi.org/10.1002/9781118437926).

- [36] S. Mallat, G. Papanicolaou, Z. Zhang, Adaptive covariance estimation of locally stationary processes, *The Annals of Statistics* 26 (1) (1998) 1–47. doi:10.1214/aos/1030563977.
- [37] R. Anderson, M. Sandsten, Inference for time-varying signals using locally stationary processes, *Journal of Computational and Applied Mathematics* 347 (2019) 24–35. doi:10.1016/j.cam.2018.07.046.
- [38] W. Martin, P. Flandrin, Wigner-Ville spectral analysis of nonstationary processes, *IEEE Transactions on Acoustics, Speech, and Signal Processing* 33 (6) (1985) 1461–1470. doi:10.1109/tassp.1985.1164760.
- [39] K. Grochenig, *Foundations of Time-Frequency Analysis*, Birkhauser, Boston, 2001.
- [40] B. Vidakovic, *Statistical Modeling by Wavelets*, John Wiley and Sons, 2009.
- [41] C. Chiann, P. A. Morettin, A wavelet analysis for time series, *Journal of Nonparametric Statistics* 10 (1) (1998) 1–46. doi:10.1080/10485259808832752.
- [42] R. B. Govindan, S. Kota, T. Al-Shargabi, A. N. Massaro, T. Chang, A. du Plessis, Effect of electrocardiogram interference on cortico-cortical connectivity analysis and a possible solution, *Journal of Neuroscience Methods* 270 (2016) 76–84. doi:10.1016/j.jneumeth.2016.06.009.
- [43] J. P. Lundgren, Computerized EEG: Applications and Interventions:, *Journal of Neuroscience Nursing* 22 (2) (1990) 108–112. doi:10.1097/01376517-199004000-00010.
- [44] L. Hu, Z. Zhang (Eds.), *EEG Signal Processing and Feature Extraction*, Springer Singapore, Singapore, 2019. doi:10.1007/978-981-13-9113-2.
- [45] A. S. Al-Fahoum, A. A. Al-Fraihat, Methods of EEG Signal Features Extraction Using Linear Analysis in Frequency and Time-Frequency Domains, *ISRN Neuroscience* 2014 (2014) 1–7. doi:10.1155/2014/730218.
- [46] X. Gao, W. Shen, B. Shahbaba, N. Fortin, H. Ombao, Evolutionary State-Space Model and Its Application to Time-Frequency Analysis of Local Field Potentials, *Statistica Sinica* 30 (2016). doi:10.5705/ss.202017.0420.
- [47] Y. Naderi Khojasteh far, N. Riahi Alam, M. Jalalvandi, H. Hashemi, Investigate the Frequency Spectrum of Noise Signals Affecting Synchronous Signals of fMRI and fNIRS in Resting and Moving Wrists, *Frontiers in Biomedical Technologies* (Oct. 2019). doi:10.18502/fbt.v6i3.1697.
- [48] R. Fernandez Rojas, X. Huang, J. Hernandez-Juarez, K.-L. Ou, Physiological fluctuations show frequency-specific networks in fNIRS signals during resting state, in: 2017 39th Annual International Conference of the IEEE Engineering in Medicine and Biology Society (EMBC), IEEE, Seogwipo, 2017, pp. 2550–2553. doi:10.1109/EMBC.2017.8037377.
- [49] C. Yaramothu, X. Li, C. Morales, T. L. Alvarez, Reliability of Frontal Eye Fields Activation and Very Low-Frequency Oscillations Observed during Vergence Eye Movements: An fNIRS Study, *Scientific Reports* 10 (1) (Jan. 2020). doi:10.1038/s41598-020-57597-4.
- [50] T. T.-l. Chong, K.-t. Wong, Time series properties of aggregated AR(2) processes, *Economics Letters* 73 (3) (2001) 325–332. doi:10.1016/s0165-1765(01)00504-3.
- [51] D. Dacunha-Castelle, L. J. Fermin, *Aggregation of Autoregressive Processes and Long Memory*, 2008.
- [52] K. F. K. Wong, A. Galka, O. Yamashita, T. Ozaki, Modelling non-stationary variance in EEG time series by state space GARCH model, *Computers in Biology and Medicine* 36 (12) (2006) 1327–1335. doi:10.1016/j.combiomed.2005.10.001.
- [53] H.-Y. Huang, H. Ombao, D. S. Stoffer, Discrimination and Classification of Nonstationary Time Series Using the SLEX Model, *Journal of the American Statistical Association* 99 (467) (2004) 763–774. doi:10.1198/016214504000001105.
- [54] H. Ombao, J. Raz, R. von Sachs, W. Guo, The SLEX Model of a Non-Stationary Random Process, *Annals of the Institute of Statistical Mathematics* 54 (1) (2002) 171–200. doi:10.1023/A:1016130108440.
- [55] S. Cranstoun, H. Ombao, R. von Sachs, Wensheng Guo, B. Litt, Time-frequency spectral estimation of multichannel EEG using the Auto-SLEX method, *IEEE Transactions on Biomedical Engineering* 49 (9) (2002) 988–996. doi:10.1109/TBME.2002.802015.
- [56] J. L. Harvill, P. Kohli, N. Ravishanker, Clustering Nonlinear, Nonstationary Time Series Using BSLEX, *Methodology and Computing in Applied Probability* 19 (3) (2017) 935–955. doi:10.1007/s11009-016-9528-1.
- [57] S. G. Mallat, *A Wavelet Tour of Signal Processing: The Sparse Way*, 3rd Edition, Elsevier/Academic Press, Amsterdam ; Boston, 2009.
- [58] P. Flandrin, *Explorations in Time-Frequency Analysis*, 2018, <https://doi.org/10.1017/9781108363181>.
- [59] T. Instruments, ADS1299. Low-Noise, 8-Channel, 24-Bit Analog-to-Digital Converter for Biopotential Measurements, Tech. Rep. ADS1299, Texas Instruments (Jan. 2017).

- [60] B. Lizon, Fundamentals of Precision ADC Noise Analysis, Texas Instruments, 2020.
- [61] U. Rashid, I. K. Niazi, N. Signal, D. Taylor, An EEG experimental study evaluating the performance of Texas instruments ADS1299, *Sensors* 18 (11) (2018) 3721.
- [62] H. Sherkat, M. A. Pinto-Orellana, P. Mirtaheeri, SHADE: Absorption spectroscopy enhancement with ambient light estimation and narrow-band detection, *Optik* 220 (2020) 165116.
- [63] P. Pauli, W. Lutzenberger, H. Rau, N. Birbaumer, T. C. Rickard, R. A. Yaroush, L. E. Bourne Jr, Brain potentials during mental arithmetic: Effects of extensive practice and problem difficulty, *Cognitive Brain Research* 2 (1) (1994) 21–29.
- [64] M. Tanida, K. Sakatani, R. Takano, K. Tagai, Relation between asymmetry of prefrontal cortex activities and the autonomic nervous system during a mental arithmetic task: Near infrared spectroscopy study, *Neuroscience letters* 369 (1) (2004) 69–74.
- [65] Q. Wang, O. Sourina, Real-time mental arithmetic task recognition from EEG signals, *IEEE Transactions on Neural Systems and Rehabilitation Engineering* 21 (2) (2013) 225–232.
- [66] M. Verner, M. J. Herrmann, S. J. Troche, C. M. Roebers, T. H. Rammsayer, Cortical oxygen consumption in mental arithmetic as a function of task difficulty: A near-infrared spectroscopy approach, *Frontiers in human neuroscience* 7 (2013) 217.
- [67] F. Scholkmann, M. Wolf, General equation for the differential pathlength factor of the frontal human head depending on wavelength and age, *Journal of Biomedical Optics* 18 (10) (2013) 105004. doi:10.1117/1.jbo.18.10.105004.
- [68] S. Prael, Tabulated Molar Extinction Coefficient for Hemoglobin in Water, Tech. rep., Oregon Medical Laser Center, <https://omlc.org/spectra/hemoglobin/summary.html> (1998).
- [69] D. L. Schacter, EEG theta waves and psychological phenomena: A review and analysis, *Biological Psychology* 5 (1) (1977) 47–82. doi:10.1016/0301-0511(77)90028-x.
- [70] W. Klimesch, B. Schack, P. Sauseng, The Functional Significance of Theta and Upper Alpha Oscillations, *Experimental Psychology* 52 (2) (2005) 99–108. doi:10.1027/1618-3169.52.2.99.
- [71] G. Sammer, C. Blecker, H. Gebhardt, M. Bischoff, R. Stark, K. Morgen, D. Vaitl, Relationship between regional hemodynamic activity and simultaneously recorded EEG-theta associated with mental arithmetic-induced workload, *Human Brain Mapping* 28 (8) (2007) 793–803. doi:10.1002/hbm.20309.
- [72] R. H. Grabner, B. D. Smedt, Oscillatory EEG Correlates of Arithmetic Strategies: A Training Study, *Frontiers in Psychology* 3 (2012). doi:10.3389/fpsyg.2012.00428.
- [73] S. Hori, A. Seiyama, Regulation of cerebral blood flow during stimulus-induced brain activation: Instructions for the correct interpretation of fNIRS signals, *The Journal of Physical Fitness and Sports Medicine* 3 (1) (2014) 91–100. doi:10.7600/jpfsm.3.91.
- [74] M. A. Yucel, J. Selb, C. M. Aasted, P.-Y. Lin, D. Borsook, L. Becerra, D. A. Boas, Mayer waves reduce the accuracy of estimated hemodynamic response functions in functional near-infrared spectroscopy, *Biomedical Optics Express* 7 (8) (2016) 3078. doi:10.1364/boe.7.003078.